From transparent to black amorphous zinc oxide thin films through oxygen deficiency control

Magdalena Nistor, Florin Gherendi, Daniela Dobrin, Jacques Perrière

J. Appl. Phys. 132, 225705 (2022); https://doi.org/10.1063/5.0129135

From transparent to black amorphous zinc oxide thin films through oxygen deficiency control

Magdalena Nistor [1]*, Florin Gherendi[1], Daniela Dobrin[1] and Jacques Perrière [2,3]

[1] National Institute for Lasers, Plasma and Radiation Physics (NILPRP), L22 P.O. Box. MG-36, 77125 Bucharest - Magurele, Romania.

[2] Sorbonne Universités, UPMC Univ Paris 06, UMR 7588, INSP, F-75005, Paris, France ;

[3] CNRS, UMR 7588, INSP, F-75005, Paris, France.

*Author to whom correspondence should be addressed: mnistor@infim.ro; magda.nistor@inflpr.ro

ABSTRACT

Despite the fact that zinc oxide is a well-known transparent oxide, several recent studies on "black" ZnO have renewed its potential for photocatalytic applications. We report on the control of oxygen deficiency in ZnO thin films grown at 300 ºC on c-cut sapphire single-crystal substrates by pulsed electron beam deposition (PED) through a slight variation of argon pressure in PED. At a pressure of 2 10^{-2} mbar transparent, stoichiometric (ZnO) and crystalline films are obtained, while at 9 10^{-3} mbar black, oxygen-deficient ($ZnO_{0.85}$) and amorphous films result. Stoichiometry, structural and optoelectronic properties of transparent and black ZnO thin films were comparatively analysed as function of oxygen deficiency. The black ZnO thin films exhibit enhanced absorption in the visible and near-infrared due to oxygen deficiency, thus extending the range of applications of zinc oxide thin films from transparent electronics to solar absorbers and photocatalysis.

I. INTRODUCTION

Zinc oxide has attracted substantial research as n-type transparent conducting oxide due to its versatile physical and chemical properties, spanning the whole range from conductor to semiconductor behaviour, not only in the bulk but also as thin film or as various nanostructured morphologies for solar cells, optoelectronics, gas sensors, photocatalysis, etc. [1-4]. On the other hand, amorphous oxide semiconductors like In-Ga-Zn-O are widely employed in recent years as transparent thin film transistors for circuits, devices, display and memory applications due to their outstanding electrical and optical properties in the amorphous phase compared to amorphous Si [5]. Such amorphous films offer several advantages over crystalline films, e.g., a deposition temperature at or near room temperature leading to a better compatibility with flexible substrates and a reasonably high carrier mobility for applications due to the absence of grain boundaries [5].

In this context, obtaining amorphous zinc oxide films would certainly be of great interest for a lot of applications [6-14]. However, the main impediment in the formation of amorphous ZnO films is the facile crystallization of the film in the hexagonal würtzite (P63mc) structure or its nano-structuring even at or near room temperature on a wide variety of substrates [15,16]. This leads to polycrystalline ZnO thin films with electron mobility considerably limited by dislocations or impurities at the grain boundaries. Different approaches have been used to obtain the amorphous phase in zinc oxide films and to remove grain boundaries by deposition in chemical solution [6,7] growth by PLD, sputtering at cryogenic temperatures [8-10] or growth on specific substrates (paper, mylar) [11].

While transparent zinc oxide films are currently obtained by a wide variety of growth methods, black zinc oxide films are not so currently observed and investigated. Recently, black (002) ZnO samples (powders) were obtained from solution followed by a physicochemical reduction technique [17]. Zn-rich ZnO black films were also obtained by a modified magnetron sputtering method [18]. In both references [17,18], diffraction measurements showed the formation of the

wurtzite ZnO structure with a weak Zn metal phase, while in [18] XPS analysis confirmed the existence of the Zn metal phase in the film bulk but not on the film surface. Black ZnO films were also obtained by electrochemical oxidation of the Zn foil [19,20], and sol-gel method [21]. Dark nanoporous [22] and nanostructured ZnO films were synthetized by anodic oxidation of metallic zinc [23], with the presence of zinc nanoparticles in the dark-colored anodic films [14].

The aim of the present work was to investigate black ZnO films in comparison to transparent ones in terms of the role of the stoichiometry on their electrical and optical properties. We have grown these zinc oxide films by the pulsed electron beam deposition (PED) obtaining a strong change in the optical appearance of the zinc oxide films with a relatively small change in the working pressure.

The PED method has been already used for the successfully growth of pure or doped ZnO films [25-26], and other oxide films like $LaSrMnO_3$ [27], In_2O_3 [28], $LaFeO_3$ [29] and even super lattices [30]. PED is a growth method similar to PLD but using a pulsed electron beam instead of a nanosecond UV laser to ablate the target material [31, 32]. PED is a different method from electron beam evaporation because the electron beam in PED is pulsed and very intense, polyenergetic [31], having enough energy to ablate, i.e. melt, vaporize and generate an ablation plasma from a target [32]. Indeed, PED is a versatile technique due to the facile tuning of the deposition parameters (gas pressure and energy of the species) [31-34], that allows the control of the films' composition, morphology, thickness, and physical properties.

The zinc oxide films were grown in a narrow window of argon gas pressure, i.e. $9\ 10^{-3}$ mbar and $2\ 10^{-2}$ mbar denoted LP and HP respectively. Such growth conditions lead to the formation of amorphous oxygen deficient, black, zinc oxide film in the first case (LP), and crystalline, stoichiometric, transparent ZnO films in the second one (HP). The composition, morphology, structure and physical properties of the amorphous and stoichiometric films were investigated in detail and are presented and discussed comparatively.

II. EXPERIMENTAL SETUP

PED method uses the same deposition geometry for the thin film growth as in a typical PLD setup as shown in the Fig. 1. The pulsed electron beam which propagates in a self-focused way towards the target, interacts with the target at 45 degrees, then an ablation plasma is formed and propagates toward the substrate. The pulsed electron beam used for the ZnO film growth has been produced in a channel-spark discharge [31-34]. An external capacitor (16 nF) charged at 15 kV is discharged between a hollow cathode and a grounded anode (the vacuum chamber) through a capillary tube of 6 mm diameter and 140 mm length. The pulsed beam is produced having about 100 ns FWHM and a fluence of about 2.5 J/cm^2; and is incident on the ZnO target at 45 degrees. The sapphire substrate is positioned relative to the target directly below it and parallel to the target. In these experiments the substrate was placed at 4 cm from the target.

The energetic electrons in the beam are generated at the beginning of the electron beam pulse and they are followed by beam electrons of decreasing energies, i.e. a polyenergetic electron beam [31]. The energy of the pulsed electron beam in interaction with a target is mainly converted in heat, contributing to melting, vaporization and generation of the ablation plasma [32]. A small fraction of the electrons interacting with the target can be scattered from the target in all directions but not focalized like in a beam, therefore only a very small fraction of them could hit the substrate but without significantly affecting the film deposition.

All the zinc oxide films were grown on c-cut sapphire single crystal substrates, under two different argon pressures, either the 9 x 10^{-3} mbar low pressure (LP), or the 2 x 10^{-2} mbar high pressure (HP). The substrate temperature was fixed at 300°C, and the repetition rate was about 1 Hz. The important advantage of the PED method is that the composition, microstructure and the electrical and optical properties can be tuned by the growth system partial gas pressure and energy of species during film growth [31-34].

Physical and chemical analysis tools were used to investigate the films in a non-destructive way. The thickness and composition of the ZnO thin films were determined by Rutherford backscattering spectrometry (RBS), using the 2 MeV Van de Graaff accelerator of the INSP, Sorbonne Université.

X-ray photoelectron spectroscopy (XPS) measurements of black and transparent ZnO thin films were performed *ex-situ* by the Thermo Scientific ESCALAB Xi+ spectrometer at NILPRP equipped with a monochromatic Al Kα (1486.6 eV) x-ray source and using a 900 µm beam spot. The survey spectra were collected with pass energy of 100 and 1 eV energy step size. The high-resolution spectra of the Zn 2p, Zn 3p, Zn LMM, O 1s, C 1s core levels were collected with 20 eV pass energy and 0.1 eV energy step size, while for the valence band spectra the pass energy was 1 eV and 0.05 eV energy step size. Zn 3p and Zn LMM spectra were also recorded for a metallic Zn sample. All spectra were recorded before and after etching for 60 s by a 2 keV argon ion beam and compensate for electrical charging with the electron flood source. The Thermo Scientific Avantage software was used for spectra analysis.

The structural characterizations were carried out by X-ray diffraction (XRD) analyses using a four-circle diffractometer (Philips Xpert MRD) with the Cu Kα radiation ($\lambda = 0.154$ nm) The nature of the crystalline phases, their axes parameters and their eventual crystallographic textures were investigated in the symmetric Bragg-Brentano geometry.

The ZnO film resistivity from room T down to liquid helium was measured in the classical four probe geometry. The nature, mobility and density of carriers were determined using Hall method with a MMR Technologies, Inc. Hall setup at a magnetic field of 3300 G. The optical transmission of films in the range 200 - 3200 nm was measured with a Cary 5000 spectrophotometer.

III. RESULTS AND INTERPRETATIONS

A. Composition

The zinc oxide films grown under 9 10^{-3} mbar (LP) and 2 10^{-2} mbar (HP) present a drastic difference in their optical appearance, as shown in Fig. 2, where illustrative photographs are shown. Indeed, the zinc oxide films grown under the higher-pressure HP are transparent, while those grown at the lower pressure LP is black, indicating that their optical absorption changes significantly.

RBS was used to determine the composition and thickness of the transparent and black zinc oxide films. Fig. 3 shows the two representative RBS spectra corresponding to the LP and HP ZnO films. This RBS analysis demonstrates that both films have a uniform in-depth distribution of Zn and O species, without any measurable amounts of other elements. In addition, interdiffusion was not observed between the film and substrate.

The use of RUMP software revealed several insights about the films. Firstly, the thickness and composition of the films were deduced and are presented in the Table I together with electrical measurements. A first noticeable difference between these films concerns their thickness, i.e. 120 nm for the LP film, and 47 nm for the HP film. This approximately 2.5-fold difference in film thickness is significant, despite the limited difference in growth pressure and is due to the pressure dependence of the pulsed electron beam generation and gas scattering [28, 31]. Secondly, an important difference was observed in terms of film composition. For the HP film, a composition close to the stoichiometry ($ZnO_{1.02}$) was obtained within the precision of the RBS analysis. A stoichiometric zinc oxide film is grown in these conditions, as it has been generally observed [25]. On the contrary, the LP film shows a large oxygen deficiency: $ZnO_{0.85}$. This high oxygen deficiency, about 15%, is at the origin of its black (dark) colour, as shown in Fig. 3, and is present throughout the thickness of the film, as deduced from the interpretation of the RBS spectrum. Indeed, both the gradual decrease of the oxygen content of an oxide film and its thickness leads first to a grey, dark grey and then to a black colour, as observed in various oxide films obtained by different methods [17-24].

The LP film shows a large oxygen deficiency ($ZnO_{0.85}$), while zinc oxide is a material which does not present any thermodynamically stable sub-oxides. This means that the LP film with a

$ZnO_{0.85}$ composition is not stable. In fact, such a large sub-stoichiometry will lead to a phase separation with Zn clusters embedded in a stoichiometric ZnO matrix as it was previously described in other systems [35 - 45]. The disproportionation reaction leading to the complete phase separation is the following:

$$ZnO_{0.85} \rightarrow 0.85\ ZnO + 0.15\ Zn \qquad (1)$$

Since the most stable phase is the stoichiometric ZnO, this phase will grow at the expense of the remaining ZnO_x sub-oxide which becomes more and more deficient, and in the complete phase separation Zn clusters are created in the stoichiometric matrix [45]. In our present case, the disproportionation is probably not complete and a partial disproportionation in the LP film would be characterized by the following reaction:

$$ZnO_{0.85} \rightarrow aZnO + bZnO_y + cZn \qquad (2)$$

with $a + b + c = 1$ and $(a + by) = 0.85$.

Three phases will be present in the film: stoichiometric ZnO, oxygen deficient ZnO_y, and Zn clusters. It must be noticed that the presence of metallic clusters in largely oxygen deficient oxide films have been already reported in Ga_2O_x [35], ITO [38 - 41] and ZnO [45]. The phase separation occurs in largely oxygen deficient oxides which do not possess stable sub-oxides.

An interesting point is to compare the deposition rate at two pressures, which is higher for the ZnO black films (0.06 nm/s) than for those transparent (0.02 nm/s). One possible explanation is related to a specific characteristic of PED, namely that the electron energy distribution of the pulsed electron beam plays an essential role for the ablation of the target material [31-34]. This electron energy distribution of the beam depends on the working pressure for a fixed high voltage: at a higher pressure, HP, the density of low-energy electrons in the beam increases significantly at the expense of the high-energy electrons [31,32], leading to a smaller ablated volume of the target, leading to a lower deposition rate. In contrast, at a lower pressure, LP, the number of high-energy electrons increases relative to the low energy electrons leading to a higher deposition rate.

Even though irradiating the ZnO target with a high fluence UV laser (in the case of PLD) or pulsed electron beam (in the case of PED) could lead to a darkening of the ZnO target surface, not only the target atoms carried by the ablation plasma but also the oxygen atoms in the gas contribute to film formation on the substrate, leading to stoichiometric or oxygen deficient films, depending on the growth pressure.

B. X-ray diffraction

The crystalline structure of the films was investigated by XRD and Fig. 4 presents θ-2θ patterns recorded on the LP and HP films. For comparison purpose, the XRD pattern of a zinc oxide film grown on a c-cut sapphire substrate at 500°C under similar 2 10^{-2} mbar argon pressure is also presented (Fig. 4). Indeed, these growth conditions, at HP and higher substrate temperature, lead to an epitaxial film as it can be seen in the pole figure presented in inset of the Fig. 4. This X-ray pattern will be useful to characterize the two other diagrams. In order to compare the crystalline structure of these three films, the XRD patterns have been normalized to the film thickness. For the HP film, a peak is present at 33.8°, corresponding to the (002) ZnO, i.e., the classical texture of ZnO film grown on c-cut sapphire. In comparison to the film grown at 500°, it can be concluded that this HP film is only partially crystallized.

The X-ray diffraction diagram of the LP film does not show any reflection peak characteristic of the ZnO würtzite indicating that this film can be considered as nanocrystalline or amorphous. This point is *a priori* rather surprising by considering the growth conditions. Indeed, the ZnO thin films were grown on c-cut sapphire substrates because those are known to favour a (002) growth for the ZnO film [16, 25, 26] even at room temperature. Despite these favourable conditions for a crystalline growth, the black LP ZnO thin films are nanocrystalline or amorphous. The increase of the film non-stoichiometry could contribute to the reduction of the crystallinity of films until amorphization.

The reason of the difference between the structure of LP and HP films, is related to the film growth process in PED. In PED, the kinetic energy of the species emitted by the target can be tailored in the range of tens of eV depending on the growth parameters. A lower deposition rate and kinetic energy of the species will allow the formation of crystalline material, as observed in the HP film. A deposition rate more than 2.5 times higher and a species kinetic energy higher than in the HP case may not be sufficient to explain amorphous film formation in the case of LP film. An obvious factor would be the high oxygen deficiency of the LP film ($ZnO_{0.85}$), which does not allow the formation of pure ZnO crystallites, leading to significant deformation of the structure.

C. Resistivity

The resistivity ρ, carrier density n and mobility μ of the LP black HP transparent Zn oxide films were determined by Hall measurements at room temperature, and summarized in Table I.

All the films have a n-type behaviour, as anticipated for un-doped zinc oxide films, and the slight difference in the growth pressure leads to evident differences in the measured Hall data. The polycrystalline and transparent ZnO films have a resistivity about ten times lower, the carrier density is two times lower while the mobility of the electron carriers is five times higher than those corresponding to the amorphous black film. The low value of mobility for the LP film would be due to the formation of a nanocomposite film with Zn clusters embedded in the oxygen-deficient oxide matrix. Some oxygen deficiencies and metal clusters could act as electron donors but also as free electron scattering centers in such a nanocomposite LP film that will lead to a large decrease of their mobility by comparison to that of the HP film. The lower carrier free mobility value for the LP film may also be indicative of the limited percolation-like network of Zn clusters. Moreover, studies on the effect of the atomic structure on the electron transport properties of ZnO thin films have proved that the electron mean free path that contribute to electrical conduction are rather limited in amorphous ZnO films compared to crystalline ZnO films due to the structural disorder as seen by X-ray absorption near edge structure (XANES) measurements [12,13]. The decrease in mobility can

also be explained by the decrease in the hybridization power of the Zn-4s and O-2p orbitals and this may limit the electron mean free path [12,13].

In the Table I are also given the values of the parameter $k_F\Lambda$ for these films described by formula (3):

$$k_F\Lambda = \hbar(3\pi^2)^{\frac{2}{3}}/(e^2\rho n^{\frac{1}{3}}) \qquad (3)$$

with Λ the electronic mean free path, k_F the Fermi momentum, n carrier density, ρ resistivity and $\hbar$ reduced Planck constant [28, 46, 47]. The value of $k_F\Lambda$ allows to characterize the nature of the electrical conduction in a film. If $k_F\Lambda << 1$ the film stands on the insulating side of the Mott metal-insulator transition (MIT) with strongly localized electrons, whereas $k_F\Lambda >> 1$ the film stays on the metallic side of the MIT [28, 46, 47]. The Table I shows that the HP film is on the metallic side of the MIT with $k_F\Lambda$ about 7. On the other hand, the $k_F\Lambda$ value equal to 0.27 for the LP film means that this film is close to the MIT transition.

To further analyse, the temperature resistivity curves $\rho(T)$ were measured for the HP and LP films respectively and presented in Fig. 5 and 6.

In the Fig. 5 the $\rho(T)$ of the HP transparent and stoichiometric ZnO film shows a temperature coefficient of resistance (TCR) slightly positive between 300 K and 280 K, indicating a metallic behaviour. Then in the following region (T < 280 K) a negative TCR is observed, representative of a semiconducting behaviour. However, the large values of $k_F\Lambda$ and density of charge carriers (see Table I) higher than the Mott critical charge density (~ 10^{19} cm^{-3}) indicates that the HP film presents a metallic character. This kind of $\rho(T)$ curve is typically explained by the quantum corrections to conductivity (QCC) [28, 48, 49], i.e., the weak localization (WL) and electron-electron interaction effects (EEI) which occur in disordered metallic oxide systems. This feature of the $\rho(T)$ has been widely reported for pure or doped Zn oxide films [46, 48, 49], and other oxide films presenting a structural disorder and a high density of carriers [28].

The least-squares fit of the $\rho(T)$ (solid line) in the region between 275 to 15 K range was performed using the three-dimensional QCC formula described in [46, 48, 49] and their fitting

parameters are presented in Table II. For HP films the parameter a_1 is very small compared with a_2, and it is a clear indication that the EEI is the main contributor for the transport in HP films.

In the lower range of temperature (4 - 15 K) the ρ(T) curve cannot be correctly fitted by the QCC formula. In the inset of the Fig. 5, a linear fit of the resistivity in this region as function of the logarithmic variation of temperature matches the 2D weak localization effect (2D WL) [50].

In the Fig. 6 the LP, film shows a ρ(T) curve with a negative TCR between 300 K and 5 K. However, as in the case of the HP film, the large carrier density (Table I) of the LP films indicates that this film also presents a metallic character and the semiconducting-like shape observed in Fig. 6 is the result of the large disorder in a metallic-like material. In the same way as for the transparent HP film, the least-squares fit of the resistivity (solid line) was carried out by QCC model in the region between 100 and 300 K and the corresponding parameters are shown in Table II. In contrast to the HP film, for p=3 (electron-phonon interactions) the a_2 coefficient controls the QCC suggesting that the WL is the main contributor for the transport in LP films, EEI being negligible in respect with the WL term.

At temperatures lower than 100 K the best fit is obtained by using the Mott variable range hopping (VRH) transport model [51] based on the strong localization of carriers, as shown in Fig. 6 (blue solid line), i.e., a fit based on the following formulae (4):

$$\rho(T) = \rho_0 e^{\left(\frac{T_{Mo}}{T}\right)^{1/4}} \qquad (4)$$

Since the role of high oxygen deficiency is reflected in the X-ray diffraction amorphous structure of LP black films, this structural disorder selectively reduces the hopping probability, which leads to conduction band localization and explains the degradation of electrical properties compared to crystalline zinc oxide HP films [13]. Moreover, while it could be expected that the presence of Zn clusters in the LP film will induce a decrease of its resistivity, this is not the case. Indeed, the resistivity increase of the LP film may be due to the semiconducting or even insulating properties of the Zn clusters of small size which has been already reported [52, 53].

D. Optical Properties

The films grown under HP and LP conditions present a colour change from transparent to almost black (Fig. 2) and Fig. 7a shows their transmission in the 200-3200 nm range. The transparency of the double polished c-cut sapphire single crystal substrate is also shown in the same Fig. 7a.

Compared with HP film, which shows values of the transparency over 85%, including that of the substrate, the LP black film exhibits a drastic decrease of the transparency, less than 40% in the visible and near-infrared regions. Similar colour changes were reported for black hydrogenated titania for which the band gap decreased from 3.3 to 1.54 eV by the introduction of interstitial hydrogen [54] and for the black zirconia whose band gap was reduced from 5.09 to 1.52 eV [55].

The optical bandgap (E_g) was calculated from Tauc's plot (Fig. 7b), i.e. $(\alpha E)^2$ vs. E, where E is the photon energy. The optical band gap values are 3.28 eV for transparent HP films and 2.95 eV for the black LP films respectively. The reducing of band gap for the black LP films is correlated to the enhancement of the optical absorption in the visible and near-infrared regions, which is favourable to the catalytic activity for hydrogen production [18]. If we consider that the Zn clusters in LP film have a size of 5 nm and few up to 30 nm as already reported for other oxides with large oxygen deficiency [39], then the Mie scattering tends to Rayleigh approximation in our case, with no significant dependence on the cluster size, because they are much smaller than the wavelength of the light, thus the Tauc formalism could be used.

The typically reported band gap values for transparent, crystalline and stoichiometric ZnO lies between 3.25 and 3.30 eV [1, 2], in good agreement with the present work. Concerning the amorphous and stoichiometric zinc oxide thin films, the values of the band gap were reported higher than 3.3 eV for films grown at cryogenic temperatures, some other films being highly transparent in the visible light range (≈87%) with an optical bandgap of 4.65 eV and an additional band edge absorption feature at 3.50 eV [9] or with a value of 3.78 eV [10]. For the black ZnO films reported

in [17] a bandgap reduction from 3.15 to 2.52 eV for white and black (002) ZnO samples was obtained from Tauc plots. In [18] the values of the bandgap were 3.18 eV for the stoichiometric ZnO thin films and decreased to 3.09-3.18 eV for films with intermediate optical transmission, while no bandgap could be measured for black samples. In the present work, the 2.95 eV band gap value is probably not due to the amorphous structure of the LP film. The origin of this narrow band gap is likely related to the large oxygen deficiency in the film as it has been previously reported [3, 56] and metal clusters, as both may be a source of subgap states as shown by density functional theory calculation in the case of In_2O_x [65].

E. X-ray photoelectron spectroscopy

XPS spectra were recorded for characterization of chemical bonding states of elements in near-surface regions (i.e., up to depths of about 10 nm) of ZnO thin films. The survey spectra of films deposited under HP and LP are very similar (not shown here) and exhibit typical peaks related to elements of ZnO and no sample contamination was found apart from a small adventitious C 1s and Ar (from etching process) emission detected. To gain more insights, high resolution core level spectra of Zn 2p, Zn LMM and O 1s and valence band (VB) spectra, were measured on HP and LP thin films and presented in Fig. 8 and 9.

M.C. Biesinger et al [58] observed that the binding energy of the Zn $2p_{3/2}$ zinc oxide peak (1021.7 eV) is too close to the binding energy of the Zn(0) metal peak (1021.4 eV), which complicates the interpretation of XPS spectra in mixed metal-oxide systems. For comparison, Fig. 8a shows Zn 2p spectra for transparent HP and black LP zinc oxide thin films, while a spectrum of a metallic Zn sample has also been recorded and plotted in the bottom graph for reference. In the case of HP and LP films, the doublet corresponds to the Zn $2p_{3/2}$ and $2p_{1/2}$ core levels of the zinc oxide. A very slight shift of 0.08 eV is observed between the HP (1022.09 eV) and LP (1022.17 eV) Zn $2p_{3/2}$ peaks, while the corresponding peak of the Zn metallic sample is shifted to the binding energy value of 1021.73 eV. In addition, the oxide peaks generally have higher FWHM than the

metal peaks, which is the case here for the Zn $2p_{3/2}$ peaks of the HP and LP films compared to the metal peak (1.60 eV LP vs 1.64 eV HP vs 0.71 eV for the Zn metallic sample).

High-resolution Zn $L_3M_{45}M_{45}$ (Zn LMM) Auger-transition spectra were recorded because Zn LMM is more sensitive than the Zn 2p spectra to changes in the oxidation state of zinc atoms [59, 60] and are shown in Fig. 8b. The Auger peaks of ZnO for LP and HP thin films have a main peak at ~498 eV (A) and a shoulder at ~495 eV (B). The binding energy of the peak A decreased from 498.5 eV to 498.4 eV with increasing the oxygen deficiency from HP to LP films. A major difference appears in the spectrum of the metallic Zn sample, peak A decreased and peak B increased significantly at ~495 eV, being a signature of the metallic Zn (Zn^0) [54].

In this case the determination of the chemical state is made typically using the modified Auger parameter α_A of the Zn element in a compound (ZnO) between the Zn $2p_{3/2}$ and Zn LMM peaks [61], which is defined as the sum of the kinetic energy of the Auger-transition line Zn LMM, E_K(LMM), and the binding energy of the core-level photoelectron line, Zn $2p_{3/2}$, E_B [62]:

$$\alpha = E_K(LMM) + E_B\left(Zn_{p_{3/2}}\right) \qquad (5)$$

The α_A values of films were determined using the peak A of Zn LMM to be 2010.33 eV (HP) and 2010.35 eV (LP), indicating the Zn (II) oxide. For the Zn metallic sample α_A was 2013.61 eV, corresponding to the metallic Zn, Zn (0). The lower α_A values indicates the higher oxidation state [62], as in the case of LP and HP films. Taking into account the shoulder B of both films, the values of α_A of these peaks increase towards approximately 2013 eV values, thus a mixed system of Zn metal and ZnO could not be excluded [58-60]. For example, the appearance of the metallic Zn phase in the bulk of a ZnO film was evidenced by XPS in Zn-rich ZnO films grown by magnetron sputtering [18], which exhibited the würtzite structure with existence of small fraction of metallic Zn phase as evidenced by X-ray diffraction analysis, while the XPS analysis confirmed the existence of the Zn metal phase in the film bulk but not on the film surface.

The asymmetric peak of the O 1s core level emission, shown in Fig. 9a is dominated by two contributions, A and B. The O1 s peak shows a low binding energy component (B) at 530.73 eV

(HP) and at 530.79 eV (LP) due to bulk oxygen, i.e., O atoms tetrahedrally coordinated to four Zn atoms. The higher energy component (A) located at 532.52 (HP) and 532.47 eV (LP), respectively is attributed to the surface defective oxygen [17-23]. The A component is more significant for black films (15.63 %) than for the transparent ones (7.94 %), and is accompanied by the decrease of the peak FWHM from 1.27 eV (HP) to 1.22 eV (LP), which means a more defective surface state for the black zinc oxide films, as already reported [17-24].

The near-surface electronic structure of n-type doped HP and LP ZnO thin films was investigated by XPS. VB-XPS spectra were recorded for HP and LP thin films and are shown in Fig. 9 b. The VB-XPS of the HP film has an overall intensity slightly higher than that of the LP film and a more pronounced ratio between peaks I and II. The VB-XPS spectra consist of Zn 3d core peak at ~11 eV (not shown), a peak I at ~7-8 eV consistent to the O 2p bonding states that hybridize mainly with the Zn 4s orbitals and a peak II at ~5.0 eV, which has been ascribed to nonbonding O 2p orbitals [12, 13, 64]. Comparative studies between amorphous and a würtzite ZnO revealed a decrease in the Zn 4s-O 2p hybridization strength and the localization of Zn 4s band as a consequence of local structural disorder, indicating limited electron mean free path in amorphous ZnO and thus decreasing the electron conduction in amorphous films than in crystalline ones, as we also noticed by electrical measurements presented above [12, 13].

For the HP film the peak I is less intense than the peak II, signifying that the transparent würtzite ZnO films present the Zn-polar face [64]. For the LP film the difference between these two peaks is very slight, indicating that the Zn- surface termination but could not be attributed to a crystallographic polarity due to the X-ray diffraction amorphous structure of the LP film, as shown in the XRD pattern (Fig. 4). As already observed [12, 13, 64], the crystallographic polarity with cationic surface termination improves the electronic transport properties compared with oxygen surface termination face or disordered terminations.

The energetic separation $E = E_V - E_F$ between the valence band maximum (E_V) and the Fermi level (E_F) in the near-surface region of films was extracted using the Kraut method [63]. The values

are about 2.96 eV for LP film and 2.94 eV for HP film. Taking the estimated energy of the optical bandgap (E_g) of 3.28 eV for HP film (Table I), the band bending (E_{bb}) value given by $E_{bb}=E_g-E-E_C$, where E_C is the energy difference between Fermi level and the conduction band minimum in the bulk, is 0.34 eV for the HP film, indicating the upward band bending.

Applications of black LP zinc oxide thin films result mainly from the poor performance of transparent, crystalline and stoichiometric ZnO in photocatalysis due to its wide band gap, which implies insufficient use of visible light. Therefore, a narrow band gap would be more advantageous for photocatalysis, and the first applied results of black zinc oxide for photocatalysis, electrocatalytic activity for the hydrogen evolution reaction, photoanodes for photoelectrochemical water splitting are promising [17-24]. Moreover, the results reported in recent years concerning the development and applications of nanomaterials may be a source of inspiration for new applications of black zinc oxide in the future [66 -76].

IV. CONCLUSION

In the paper, we have reported on the composition, structure, electrical and optical properties of zinc oxide films grown at 300 ºC on c-cut sapphire single-crystal substrates using a slight variation of the argon pressure in the PED method. Black and amorphous LP zinc oxide thin films with about 15% oxygen deficiency were obtained for the first time by PED, and their properties compared to those of HP transparent ones. Both films present a structural disorder (amorphous vs. polycrystalline) and a high density of carriers, leading to a temperature dependent resistivity behaviour specific to disordered metal oxide systems, explained by metallic conductivity and QCC (HP) or Mott VRH (LP) models. The low value of mobility of the LP films could be due at least partly by the presence of Zn clusters in this film, as also deduced from modified Auger parameter of the Zn element that indicated a mixed system of Zn metal and ZnO.

ACKNOWLEDGEMENTS

M.N., D.D. and F.G. acknowledge the financial support from National Nucleu Program LAPLAS VI-contract no. 16/2019 of the Romanian Minister of Research, Innovation and Digitization. The agreement on cooperation between the National Institute for Lasers, Plasma and Radiation Physics (NILPRP), Măgurele-Bucharest and the INSP, Université Pierre et Marie Curie-Paris 6 (now Sorbonne Universities) is also acknowledged. The RBS measurements were carried out within the cooperative structure around SAFIR (Université Pierre et Marie Curie-Paris 6). Dr. I. Enculescu is acknowledged for transmittance measurements, W. Seiler for X-ray diffraction measurements and C. Hebert for resistivity measurements.

AUTHOR DECLARATIONS

Conflict of interest

The authors have no competing interests to declare that are relevant to the content of this article.

Author Contributions

Magdalena Nistor: Conceptualization (lead); formal analysis (lead); Investigation (lead); writing – original draft (equal); Visualization (equal); writing – review and editing (lead). **Florin Gherendi:** Investigation (equal); review and editing (supporting); **Daniela Dobrin:** Visualization (equal); review and editing (supporting); **Jacques Perrière:** Conceptualization (supporting); Investigation (equal); formal analysis (supporting), Writing – original draft (equal); Writing – review and editing (equal).

DATA AVAILABILITY

The data that support the findings of this study are available from the corresponding author upon reasonable request.

REFERENCES

1 - C. Klingshirn, J. Fallert, H. Zhou, J. Sartor, C. Thiele, F. Maier-Flaig, D. Schneider, H. Kalt, 65 years of ZnO research-old and very recent results, Phys. Status Solidi **247** (2010) 1424-1447.

2 - K. Ellmer, A. Klein, and B. Rech, Editors, *Transparent Conductive Zinc Oxide* (Springer, 2008)

3 - J. Wang, R. Chen, L. Xiang, S. Komarneni, Synthesis, properties and applications of ZnO nanomaterials with oxygen vacancies: A review, Ceramics International **44** (2018) 7357-7377

4 - R.A. Afre, N. Sharma, M. Sharon, Transparent conducting oxide films for various applications: A review, Rev. Adv. Mat. Sci. **53** (2018) 79-89.

5 - *Amorphous Oxide Semiconductors: IGZO and Related Materials for Display and Memory*, edited by H. Hosono, H. Kumomi (John Wiley & Sons, Ltd, 2022) DOI:10.1002/978111971564

6 - N. Asakuma, H. Hirashima, T. Fukui, M. Toki, K. Awazu, H. Imai, Photoreduction of amorphous and crystalline ZnO films, Jpn. J. Appl. Phys. **41** (2002) 3909-3915.

7 - J. Tellier, D. Kuscer, B. Malic, J. Gilensek, M. Skarabot, J. Kovac, G. Goncalves, I. Musevic, M. Kosec, « Transparent, amorphous and organics-free ZnO thin films produced by chemical solution deposition at 150°C », Thin Solid films **518** (2010) 5134-5139.

8 - H.C. Tang, J. Kim, H. Hiramatsu, H. Hosono, T. Kamiya, « Fabrication and opto-electrical properties of amorphous (Zn,B)O thin film by pulsed laser deposition », J. Ceram. Soc. Jap. **123** (2015) 523-526.

9 - M. Zubkins, J. Gabrusenoks, G. Chikvaidze, J. Butikova, R. Kalendarev, L. Bikse, Amorphous ultra-wide bandgap ZnOx thin films deposited at cryogenic temperatures », J. Appl. Phys. **128** (2020) 215303.

10 - J. Bruncko, A. Vincze, M. Netrvalova, P. Sutta, D. Hasko, M. Michalka, Annealing and crystallization of amorphous ZnO thin films deposited under cryogenic conditions by pulsed laser deposition, Thin Solid Films **520** (2011) 866-870.

11 - D.J. Rogers, V.E. Sandana, F. Hosseini Teherani, R. McClintock, M. Razeghi, H.J. Drouhin, Amorphous ZnO films grown by room temperature pulsed laser deposition on paper and mylar for transparent electronic applications, Proc. SPIE **Vol. 7940** (2011) doi : 10.1117/12.879928.

12 - D.-Y. Cho, J.H. Kim, K.D. Na, J. Song, C.S. Hwang, B.-G. Park, J.-Y. Kim, C.-H. Min, S.-J. Oh, « Spectroscopic evidence for limited carrier hopping interaction in amorphous ZnO film », Appl. Phys. Lett. **95** (2009) 261903.

13 - D.-Y. Cho, J.H. wan Kim, C.S. Hwang, Electron hopping interactions in amorphous ZnO films probed by x-ray absorption near edge structure analysis, Appl. Phys. Lett. **98**, 222108 (2011) 222108.

14 -Y. Inoue, M. Okamoto, T. Kawahara, Y. Okamoto, J. Morimoto, Thermoelectric properties of amorphous zinc oxide thin films fabricated by pulsed laser deposition, Materials Transactions **46** (2005) 1470-1475.

15 - W. Chamorro, D. Horwat, P. Pigeat, P. Miska, S. Migot, F. Soldera, P. Boulet, F. Mücklich, "Near-room temperature single domain epitaxy of reactively sputtered ZnO films", J. Phys. D: Appl. Phys. **46** (2013) 235107.

16 - V. Craciun, J. Perrière, N. Bassim, R.K. Singh, D. Craciun,J. Spear, "Low temperature growth of epitaxial ZnO films on (001) sapphire by ultraviolet assisted pulsed laser deposition", Appl. Phys. A **69** (1999) S531-S533.

17 - A. Badreldin, A. Abdel-Wahab, P. B. Balbuena, Local Surface Modulation Activates Metal Oxide Electrocatalyst for Hydrogen Evolution: Synthesis, Characterization, and DFT Study of Novel Black ZnO, ACS Appl. Energy Mater. **3** (2020) 3, 10590-10599.

18 - S. Varnagiris, M. Urbonavicius, S. Tuckute, M. Lelis, Formation of Zn-rich ZnO films with improved bulk and surface characteristics by approach of magnetron sputtering technique, Thin Solid Films, **738** (2021) 138967.

19 - Y. Chen, P. Schneider, Bi-Ju Liu, Sergiy Borodin, Bin Ren and Andreas Erbe, Electronic structure and morphology of dark oxides on zinc generated by electrochemical treatment, Phys. Chem. Chem. Phys. **15** (2013) 9812-9822.

20 - J. Zuo, A. Erbe, Optical and electronic properties of native zinc oxide films on polycrystalline Zn, Phys. Chem. Chem. Phys. **12** (2010) 11467-11476.

21 - M. Krzywiecki, L. Grządziel, A. Sarfraz, D. Iqbal, A. Szwajca, A. Erbe, Zinc oxide as a defect-dominated material in thin films for photovoltaic applications – experimental determination of defect levels, quantification of composition, and construction of band diagram, Phys. Chem. Chem. Phys. **17** (2015) 10004-10013.

22 - K. Mika, K. Syrek, T. Uchacz, G. D. Sulka, L. Zaraska, Dark nanostructured ZnO films formed by anodic oxidation as photoanodes in photoelectrochemical water splitting, Electrochim. Acta **414** (2022) 140176,

23 - K. Mika, R.P. Socha, P. Nyga, E. Wiercigroch, K. Małek, M. Jarosz, T. Uchacz, G.D. Sulka, L. Zaraska, Electrochemical synthesis and characterization of dark nanoporous zinc oxide films**,** Electrochim. Acta **305** (2019) 349-359.

24 - R. Masuda, D. Kowalski, S. Kitano, Y. Aoki, T. Nozawa, H. Habazaki, Characterization of dark-colored nanoporous anodic films on zinc**,** Coatings **10** (2020) 1014.

25 - S. Tricot, M. Nistor, E. Millon, C. Boulmer-Leborgne, N.B. Mandache, J. Perrière, W. Seiler, Epitaxial ZnO thin films grown by pulsed electron beam deposition, Surf. Sci. **604** (2010) 2024-2030.

26 - M. Ozdogan, S. Ygen, C. Celebi, G.Utlu, The comparison of transient photocurrent spectroscopy measurement of pulsed electron deposited ZnO thin films for air and vacuum ambient, Thin Solid Films **680** (2016) 48-54.

27 - P. Graziosi, M. Prezioso, A. Gambardella, C. Kitts, R.K. Rakshit, A. Riminucci, I. Bergenti, F. Borgatti, C. Pernechele, M. Solzi, D. Pullini, D. Busquets-Mataix, V.A. Dediu, Conditions for the growth of smooth $La_{0.7}Sr_{0.3}MnO_3$ thin films by pulsed electron beam ablation, Thin Solid Films **534** (2013) 83-89.

28 - M. Nistor, F. Gherendi, J. Perrière, Degenerate and non-degenerate In_2O_3 thin films by pulsed electron beam deposition, Materials Science in Semiconductor Processing **88** (2018) 45-50.

29 - A. Cyza, A. Kopia, L. Cieniek, J. Kusinski, Structural characterization of Sr doped $LaFeO_3$ thin films prepared by pulsed electron deposition method, Materials Today-Proceedings **3** (2016) 2707-2712.

30 - M. Gu, S.A. Wolf, J.W. Lu, Transport phenomena in $SrVO_3/SrTiO_3$ Superlattices & Superstructures, J. Phys. D-Appl. Phys. **51** (2018) 10LT01.

31 - M. Nistor, N.B. Mandache, Electron energy distribution function of a pulsed intense electron beam, J. Optoel. Adv. Mat. **7** (2005) 1619-1622.

32 - M. Nistor, N.B. Mandache, J. Perrière, "Pulsed electron beam deposition of oxide films, J. Phys. D-Appl. Phys. **41** (2008) 165205.

33 - E. Dewald, M. Ganciu, N.B. Mandache, G.S. Musa, M. Nistor, A.M. Pointu, I.I. Popescu, K. Frank, D.H.H. Hoffmann, R. Stark, Role of the multielectrode geometry in the generation of pulsed intense electron beam in preionization-controlled open ended hollow cathode transient discharge, IEEE Trans. Plasma. Sci. **25** (1997) 279-283.

34 - M. Nistor,, P. Charles, M. Ganciu, M. Lamoureux, N.B. Mandache, A.M. Pointu, Electron energy distribution in a transient open-ended hollow cathode discharge, Plasma Sources Science & Technology **11** (2002) 183-189.

35 - A. Petitmangin, C.Hebert, J. Perrière, B. Gallas, L. Binet, P. Barboux, P. Vermaut, Metallic clusters in nonstoichiometric gallium oxide films, J. Appl. Phys. **109** (2011) 013711.

36 - L. Nagarajan, R.A. De Souza, D. Samuelis, I. Valov, A. Borger, J. Janek, K.D. Becker, P.C. Schmidt, M. Martin, A chemically driven insulator-metal transition in non-stoichiometric and amorphous gallium oxide, Nature Materials **7** (2008) 391-398.

37 - P.P. Murmu, A. Shettigar, S.V. Chong, Z. Liu, D. Goodacre, V. Jovic, T. Mori, K.E. Smith, J. Kennedy, Role of phase separation in nanocomposite indium-tin –oxide films for transparent thermoelectric applications, Journal of Materiomics **7** (2021) 612-620.

38 - M. Nistor, J. Perrière, C. Hebert, W. Seiler, Nanocomposite indium tin oxide thin films: formation induced by a large oxygen deficiency and properties, J. Phys. Cond. Matter. **22** (210) 04506.

39 - J. Perriere, C.Hebert, A. Petitmangin, X. Portier, W. Seiler, M. Nistor, "Formation of metallic nanoclusters in oxyygen deficient indium tin oxide films", J. Appl. Phys. 109 (2011) 123704.

40 - E. Millon, M. Nistor, C. Hebert, Y. Davila, J. Perrière, Phase separation in nanocomposite indium tin oxide thin films grown at room temperature: on the role of oxygen deficiency, J. Mater. Chem. **22,** 12179-12185 (2012).

41 - K.A. Bogle, V. Anbusathaiah, M. Arredondo, J.Y. Lin, Y.H. Chu, C. O'Neill, J.M. Gregg, M.R. Castell, V. Nagarajan, Synthesis of epitaxial metal oxide nanocrystals via a phase separation approach, ACS NANO **4** (2010) 5139-5146.

42 - T. Leichtweiss, R.A. Henning, J. Koettgen, R.M. Schmidt, B. Holländer, M. Martin, M. Wuttig, J. Janek, Amorphous and highly nonstoichiometric titania (TiOx) thin films close to metal-like conductivity, J. Mat. Chem. A **2** (2014) 6631-426640.

44 - N. Sbai, J. Perrière, W. Seiler, E. Millon, Epitaxial growth of titanium oxide thin films on c-cut and alpha-cut sapphire substrates , Surf. Sci. **601** (2007) 5649-5658.

45 - C. Cachoncinlle, E. Millon, X. Portier, C. Hebert, J. Perrière, M. Nistor, Anisotropy of physical properties in pulsed laser-deposited ZnO films. Appl. Phys. A **128** (2022) 530.

46 - M. Nistor, N.B. Mandache, J. Perrière, C. Hebert, F. Gherendi, W. Seiler, Growth, structural and electrical properties of polar ZnO thin films on MgO substrates, Thin Solid Films **519** (2011) 3959-3964.

47 - A.F. Ioffe, A.R. Regel, "Progress in Semiconductors", vol. 4 (Ed. A.F. Gibson), Wiley, New York, vol. **4** (1960) p.237.

48 - R.S. Ajimsha, A.K. Das, M.P. Joshi, L.M. Kukreja, Quantum corrections to low temperature electrical conductivity in Dy doped ZnO thin films, Thin Solid Films **589** (2015) 521-525.

49 - K. Das, R.S. Ajimsha, L.M. Kukreja, Thickness dependent metal–insulator transition and dimensional crossover for weak localization in $Si_{0.02}Zn_{0.98}O$ thin films grown by pulsed laser deposition, J. Appl. Phys. **115** (2014) 193705.

50 - P.A. Lee, T.V. Ramakrishnan, Disordered electronic systems, Rev. Mod. Phys. **57** (1985) 287-337.

51 - N.F. Mott, "Metal Insulator Transitions", Eds Taylor and Francis, London (1974).

52 - J. Wang, G. Wang, J. Zhao, Non metal-metal transition in Zn_n (n = 2-20) clusters, Phys. Rev. A **68** (2003) 013201.

53 - Y. Dai, D. Dai, B. Huang, C. Yan, Size-dependent metal-non metal change of group IB and IIB metal clusters, Eur. Phys. J. D **34** (2005) 105-107.

54 - X. Chen, L. Liu, P.Y. Yu, S.S.Mao, Increasing solar absorption for photocatalysis with black hydrogenated titanium dioxide nanocrystals, Science **331** (2011) 746−750.

55 - F. Qi, Z. Yang, J. Zhang, Y. Wang, Q.Qiu, H. Li, Interfacial Reaction-Induced Defect Engineering: Enhanced Visible and Near-Infrared Absorption of Wide Band Gap Metal Oxides with Abundant Oxygen Vacancies, ACS Applied Materials & Interfaces **12** (2020) 55417-55425.

56 - M.J. Brett, R.R. Parsons, Optical properties of nonstoichiometric zinc oxide films deposited by bias sputtering. J. Vac. Sci. Technol. A **4** (1986) 423.

57 - N.K. Divya, P.P. Pradyumnan, Photoluminescence quenching and photocatalytic enhancement of Pr-doped ZnO nanocrystals, Bull. Mater. Sci. **40** (2017) 1405-1413.

58 - Mark C. Biesinger, Leo W.M. Lau, Andrea R. Gerson, Roger St.C. Smart, Resolving surface chemical states in XPS analysis of first row transition metals, oxides and hydroxides: Sc, Ti, V, Cu and Zn, Appl. Surf. Sci. **257** (2010) 887-898.

59 - P. Wendel, S. Periyannan, W. Jaegermann, .A. Klein, Polarization dependence of ZnO Schottky barriers revealed by photoelectron spectroscopy, Phys. Rev. Materials **4** (2020) 084604.

60 - G. E. Hammer, R. M. Shemenski, The oxidation of zinc in air studied by XPS and AES, J. Vac. Sci. & Technol. A **1** (1983) 1026-1028.

61 - C. Wagner, A. Joshi, The Auger parameter, its utility and advantages: a review, J. Electron. Spectrosc. Relat. Phenom. **47** (1988), 283-313.

62 - G. Moretti, The Wagner plot and the Auger parameter as tools to separate initial- and final-state contributions in X-ray photoemission spectroscopy, Surf. Sci. **618** (2013) 3-11.

63 - J. Williams, H. Yoshikawa, S. Ueda, Y. Yamashita, K. Kobayashi, Y. Adachi, H. Haneda, T. Ohgaki, H. Miyazaki, T. Ishigaki, and N. Ohashi, Polarity-dependent photoemission spectra of wurtzite-type zinc oxide, Appl. Phys. Lett. **100** (2012) 051902.

64 - E.A. Kraut, R.W. Grant, J.R. Waldrop, and S.P. Kowalczyk, Precise Determination of the Valence-Band Edge in X-Ray Photoemission Spectra: Application to Measurement of Semiconductor Interface Potentials, Phys. Rev. Lett. **44** (1980) 1620.

65 - J. E. Medvedeva, E. Caputa-Hatley, and I. Zhuravlev, Metallic networks and hydrogen compensation in highly nonstoichiometric amorphous In_2O_{3-x}, Phys. Rev. Materials 6, 025601 (2022)

66 - Y. Cao, P. Qu, C. Wang, J. Zhou, M. Li, X. Yu, Xuan Yu, J. Pang, W. Zhou, H. Liu, and G. Cuniberti, Epitaxial Growth of Vertically Aligned Antimony Selenide Nanorod Arrays for Heterostructure Based Self-Powered Photodetector, Adv. Optical Mater. **10** (2022) 2200816.

67- Y. Cao, C. Liu, T. Yang, Y. Zhao, Y. Na, C. Jiang, J. Zhou, J. Pang, H. Liu, M. H. Rummeli, W. Zhou, and G. Cuniberti, Gradient bandgap modification for highly efficient carrier transport in antimony sulfide-selenide tandem solar cells, Sol. Energy Mater. Sol. Cells **246** (2022) 111926.

68 - G. W. Mattson, K. T. Vogt, J. F. Wager, and M. W. Graham, Hydrogen incorporation into amorphous indium gallium zinc oxide thin-film transistors, J. Appl. Phys. **131** (2022) 105701.

69 - J. Pang, Y. Wang, X. Yang, L. Zhang, Y. Li, Y. Zhang, J. Yang, F. Yang, X. Wang, G. Cuniberti, H. Liu, and M. H. Rummeli, A wafer-scale two-dimensional platinum monosulfide ultrathin film via metal sulfurization for high performance photoelectronics, Mater. Adv. **3** (2022) 1497.

70 - X. Wang, and A. Dodabalapur, Interface roughness and interface roughness scattering in amorphous oxide thin-film transistors, J. Appl. Phys. **130** (2021) 145302.

71 - S. Zhang, J. Pang, Q. Cheng, F. Yang, Y. Chen, Y. Liu, Y. Li, T. Gemming, X. Liu, B. Ibarlucea, J. Yang, H. Liu, W. Zhou, G. Cuniberti, and M. H. Rummeli, High-performance electronics and optoelectronics of monolayer tungsten diselenide full film from pre-seeding strategy, InfoMat. **3** (2021) 1455.

72 - Y. Cao, C. Liu, J. Jiang, X. Zhu, J. Zhou, J. Ni, J. Zhang, J. Pang, M. H. Rummeli, W. Zhou, H. Liu, and G. Cuniberti, Theoretical Insight into High-Efficiency Triple-Junction Tandem Solar Cells via the Band Engineering of Antimony Chalcogenides, Sol. RRL **5** (2021) 2000800.

73 - Y. Wang, Y. Zhang, Q. Cheng, J. Pang, Y. Chu, H. Ji, J. Gao, Y. Han, L. Han, H. Liu, and Y. Zhang, Large area uniform PtSx synthesis on sapphire substrate for performance improved photodetectors, Appl. Mater. Today **25** (2021) 101176.

74 - I. Maslyanitsyn, I. Hayrullina, V. Shigorin, V. Voronov, I. Nagovitsyn, V. Savranskii, N. Novikov, A. Lobanov, and G. Chudinova, Microcrystal ordering and second-order optical susceptibilities of zinc oxide films, J. Appl. Phys. **131** (2022) 053105.

75 - J. Zhou, D. Meng, T. Yang, X. Zhang, Z. Tang, Y. Cao, J. Ni, J. Zhang, Z. Hu, and J. Pang, Enhanced charge carrier transport via efficient grain conduction mode for Sb_2Se_3 solar cell applications, Appl. Surf. Sci. **591** (2022) 153169.

76 - H. Q. Ta, L. Zhao, D. Pohl, J. Pang, B. Trzebicka, B. Rellinghaus, D. Pribat, T. Gemming, Z. Liu, A. Bachmatiuk and M. H. Rummeli, Graphene-Like ZnO: A Mini Review, Crystals **6** (2016) 100.

TABLE CAPTION

Table I: Stoichiometry, thickness, deposition rate, electrical properties and band gap values of ZnO thin films grown at LP and HP, respectively

Table II: The parameters obtained from the fitting of the temperature dependent resistivity curves using the QCC model.

TABLES

	O/Zn	Thickness (nm)	Deposition rate (nm/s)	ρ (Ωcm)	μ (V/cm^2s)	n (cm^{-3})	$k_F\Lambda$	E_g (eV)
ZnO black (LP)	0.85	120	0.06	$2.164\ 10^{-2}$	0.91	$5.53\ 10^{20}$	0.27	2.95
ZnO transparent (HP)	1.02	47	0.02	$3.941\ 10^{-3}$	5.75	$2.76\ 10^{20}$	7.1	3.28

Table I

ZnO	Fit range	σ_0 ($\Omega^{-1}cm^{-1}$)	a_1 ($\Omega^{-1}cm^{-1}K^{-3/2}$)	p	a_2 ($\Omega^{-1}cm^{-1}K^{-1/2}$)	b ($\Omega^{-1}cm^{-1}K^{-2}$)
HP	15 – 275 K	218.72	0.00059	3	2.19	$8.32\ 10^{-10}$
LP	100 – 300 K	23.55	0.0053	3	$4.14\ 10^{-16}$	$2.16\ 10^{-8}$

Table II

FIGURE CAPTION

Fig. 1: Sketch of the PED deposition geometry

Fig. 2: Photos of the ZnO thin films grown on c-cut sapphire single-crystal (10 x 10 mm) at 300 °C and (a) HP (transparent) and (b) LP (black) pressures together with a centimeter scale-marker

Fig. 3: RBS spectra recorded for a LP ZnO thin film (black squares) and a HP film (red circles) grown by PED on c-cut sapphire substrate at 300 °C. The black and red line represent the fitting of the spectra.

Fig. 4 XRD patterns for the ZnO films grown by PED at LP (black line), HP (red line) at 300 °C and at HP and 500 °C (blue line) respectively on c-cut sapphire single crystalline substrates. In the inset is shown the pole figure of the (10.3) family planes of the ZnO thin film grown c-cut sapphire substrate at HP and 500 °C.

Fig. 5 Temperature dependent resistivity of the HP film (open squares). The fit (red solid line) was performed by using the QCC model. The inset shows the resistivity curve as a function of temperature in logarithmic scale and the resultant fit (solid line)

Fig. 6: Temperature dependent resistivity of the LP film (open squares). The fit (red solid line) of the resistivity curve was performed by using the QCC model. The fit (blue solid line) was performed by using the Mott VRH model

Fig. 7: (a) Optical transmittance spectra of the HP, LP zinc oxide thin films and c-cut sapphire single crystal substrate, respectively. (b) The Tauc's plot of the HP and LP zinc oxide thin films. The linear fit for the band gap estimation is presented as solid line.

Fig. 8: High-resolution X-ray photoelectron spectra of the Zn 2p region (a) and Zn $L_3M_{45}M_{45}$ Auger region (b) as recorded from HP (top), LP (middle) zinc oxide thin films and metallic Zn sample (bottom).

Fig. 9: X-ray photoelectron spectroscopy O1s core levels (a) and valence band spectra (b) of the HP and LP ZnO thin films.

FIGURES

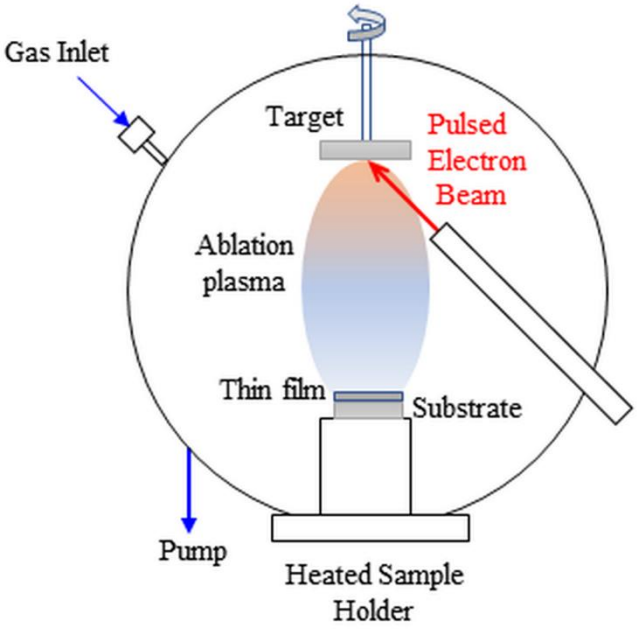

Fig. 1

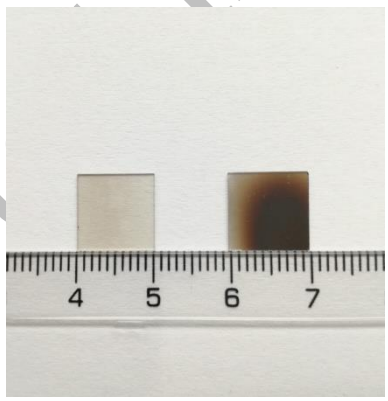

(a) (b)

Fig. 2

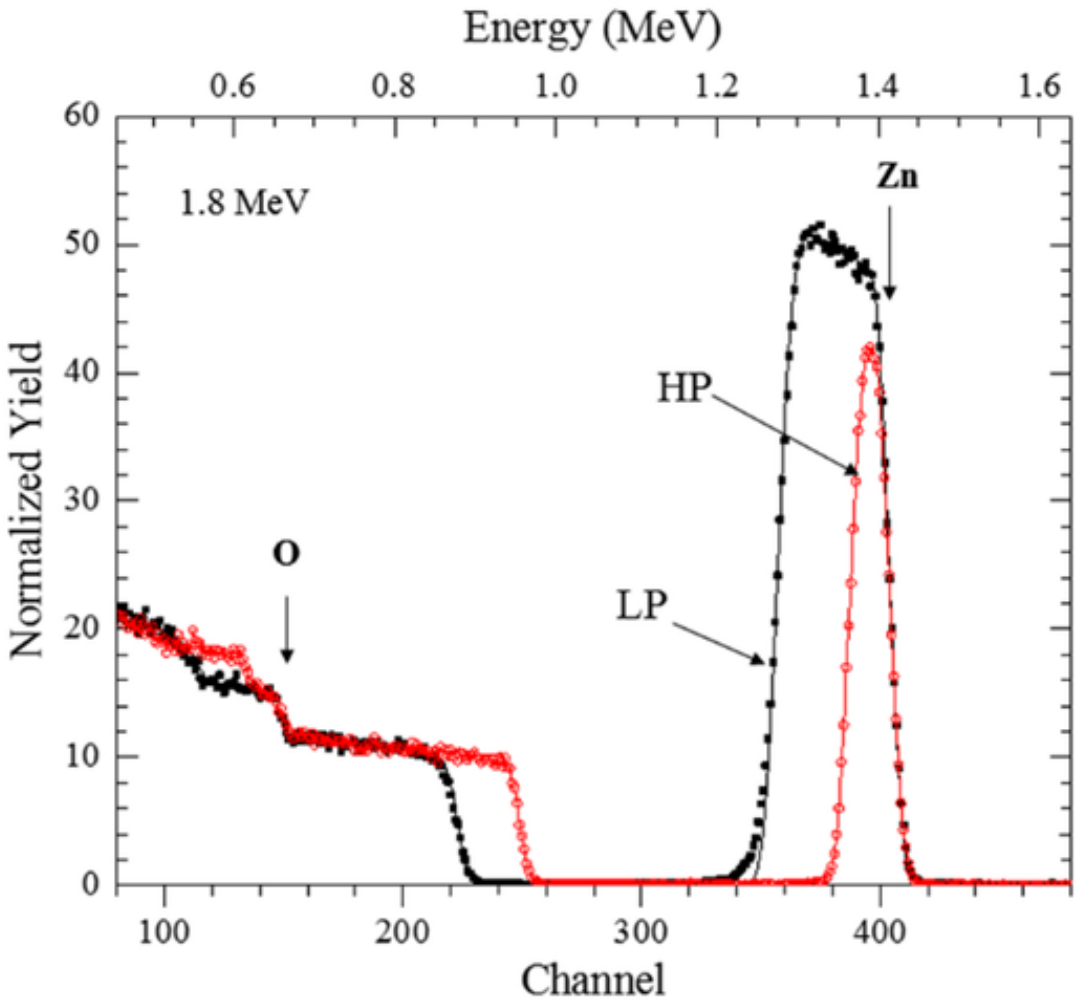

Fig. 3

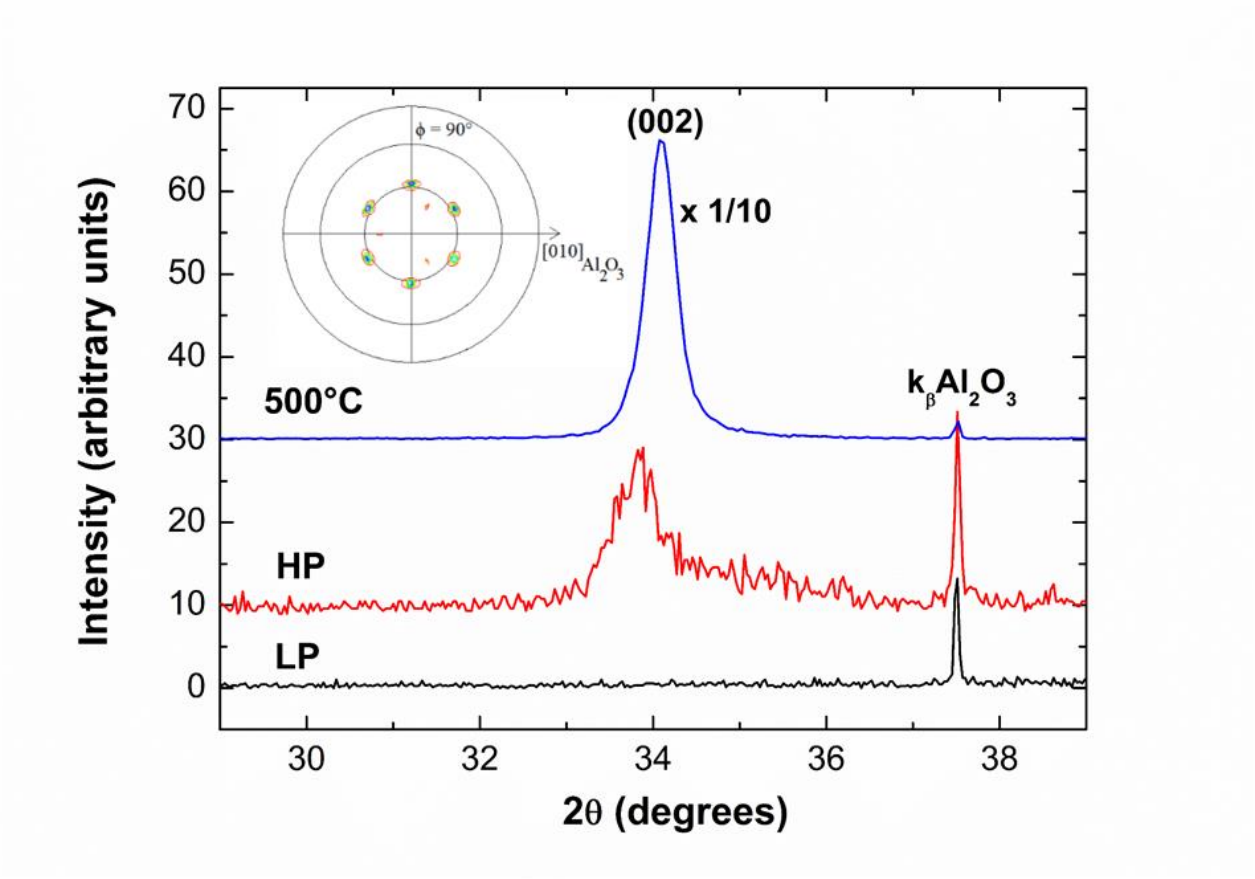

Fig. 4

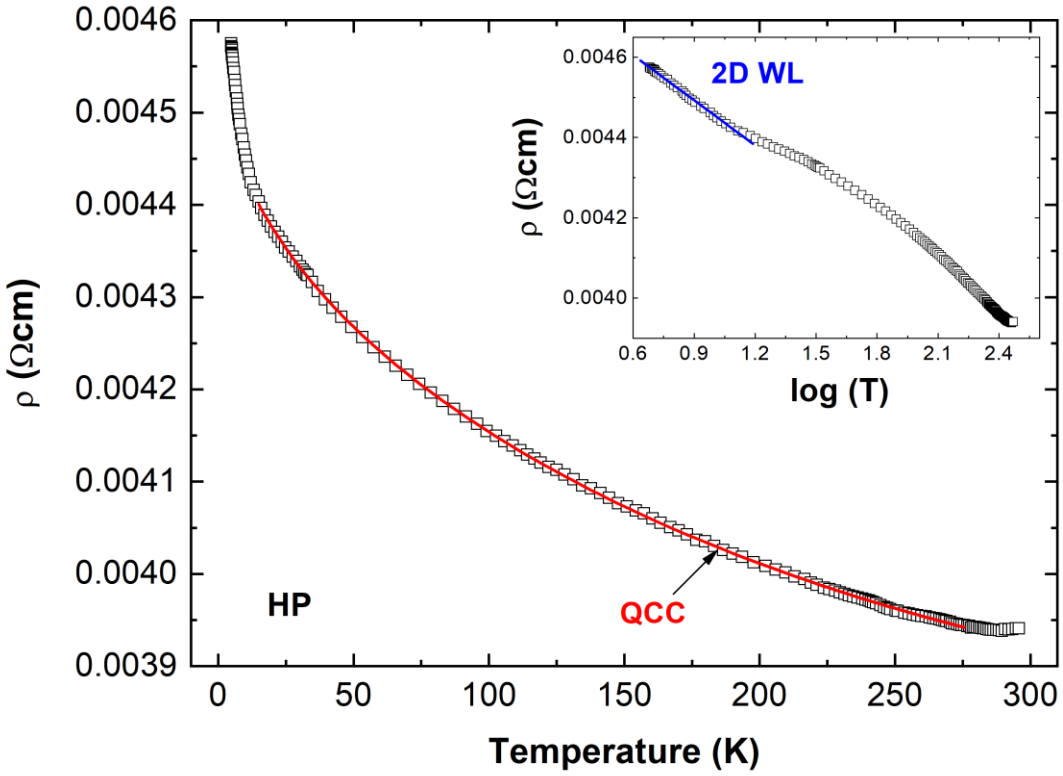
0.0046
0.0045
0.0044
0.0043
0.0042
0.0041
0.0040
0.0039
ρ (Ωcm)
0
50
100
150
200
250
300
Temperature (K)
HP
QCC
2D WL
0.0046
0.0044
0.0042
0.0040
ρ (Ωcm)
0.6
0.9
1.2
1.5
1.8
2.1
2.4
log (T)

Fig. 5

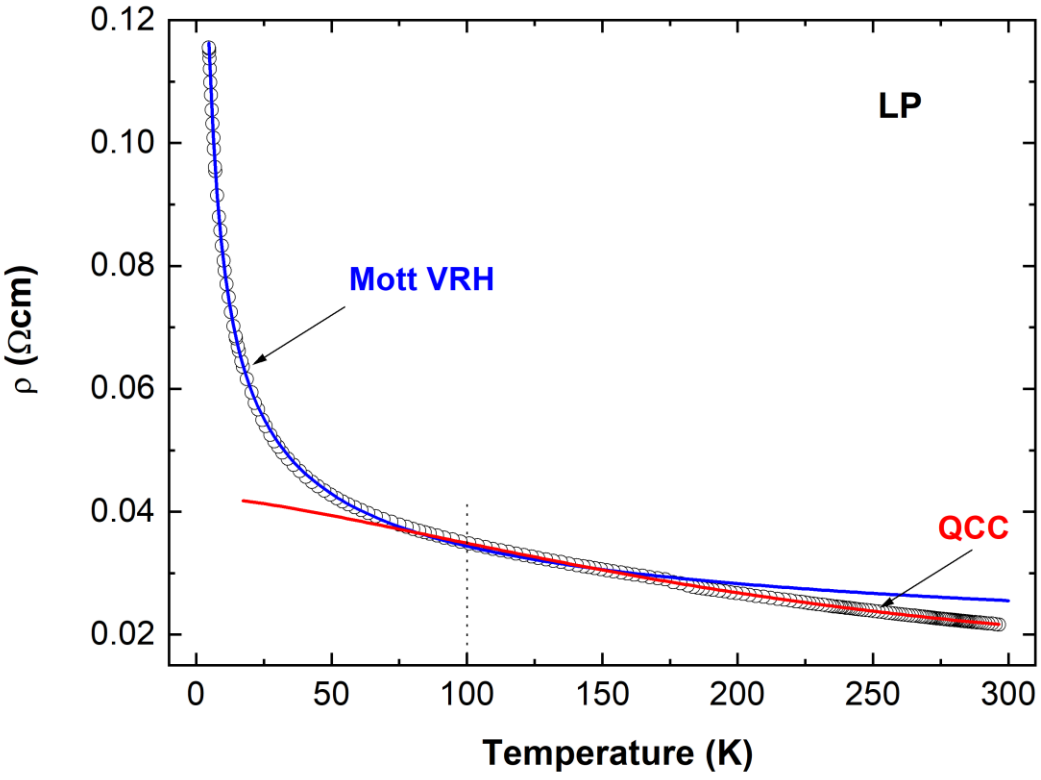
0.12
0.10
0.08
0.06
0.04
0.02
ρ (Ωcm)
0
50
100
150
200
250
300
Temperature (K)
LP
Mott VRH
QCC

Fig. 6

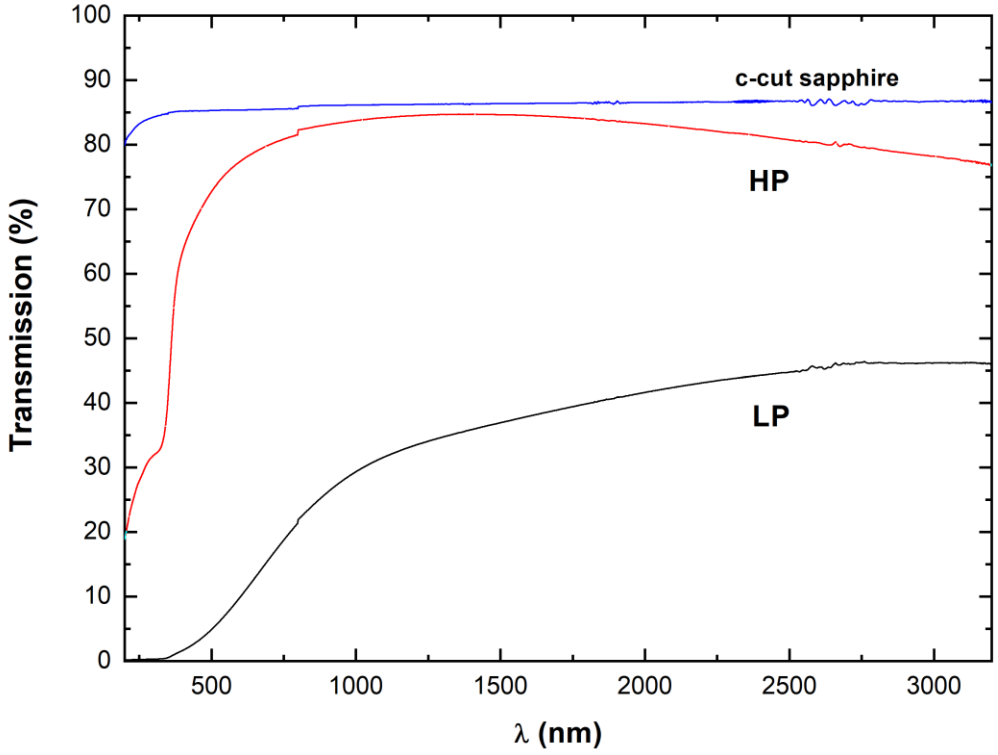
Transmission (%)
λ (nm)
c-cut sapphire
HP
LP
100
90
80
70
60
50
40
30
20
10
0
500
1000
1500
2000
2500
3000

a

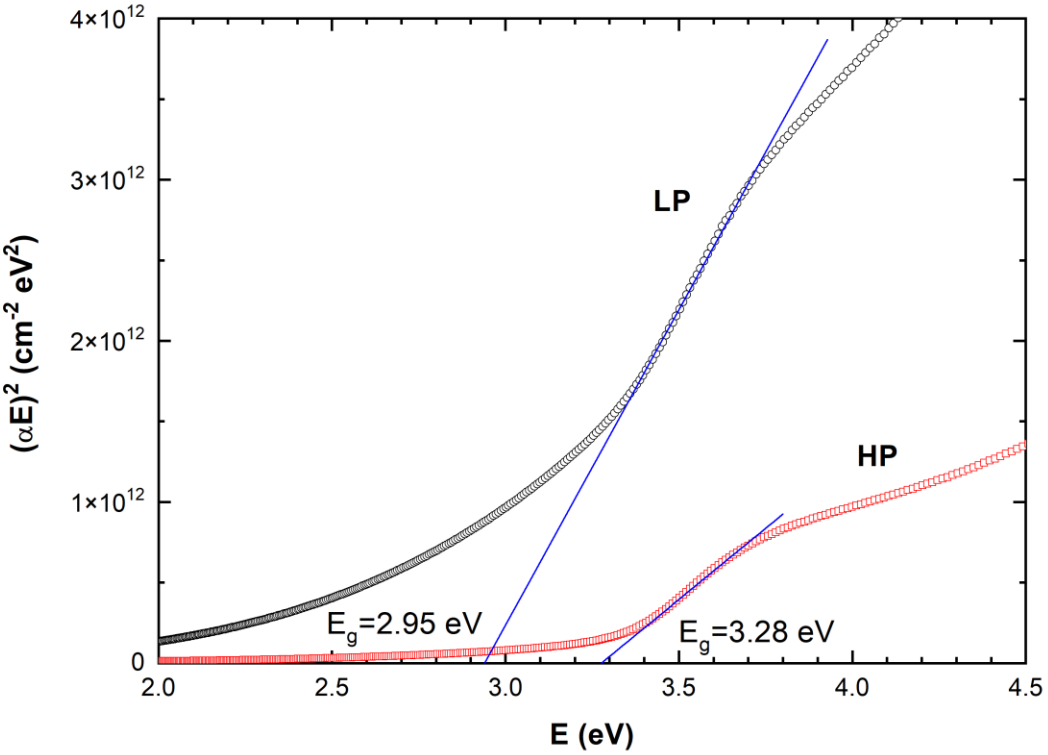
(αE)² (cm⁻² eV²)
E (eV)
LP
HP
Eg=2.95 eV
Eg=3.28 eV
4×10¹²
3×10¹²
2×10¹²
1×10¹²
0
2.0
2.5
3.0
3.5
4.0
4.5

b

Fig. 7

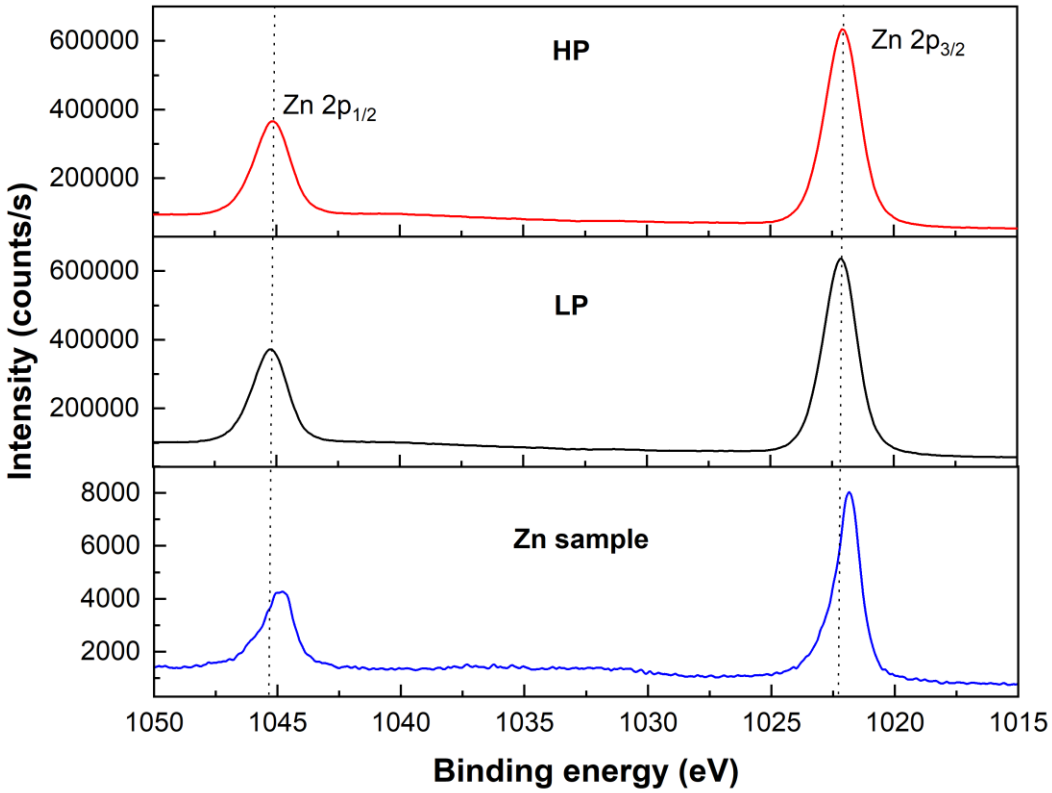
HP
LP
Zn sample
Zn 2p1/2
Zn 2p3/2
Intensity (counts/s)
Binding energy (eV)
600000
400000
200000
8000
6000
4000
2000
1050
1045
1040
1035
1030
1025
1020
1015

a

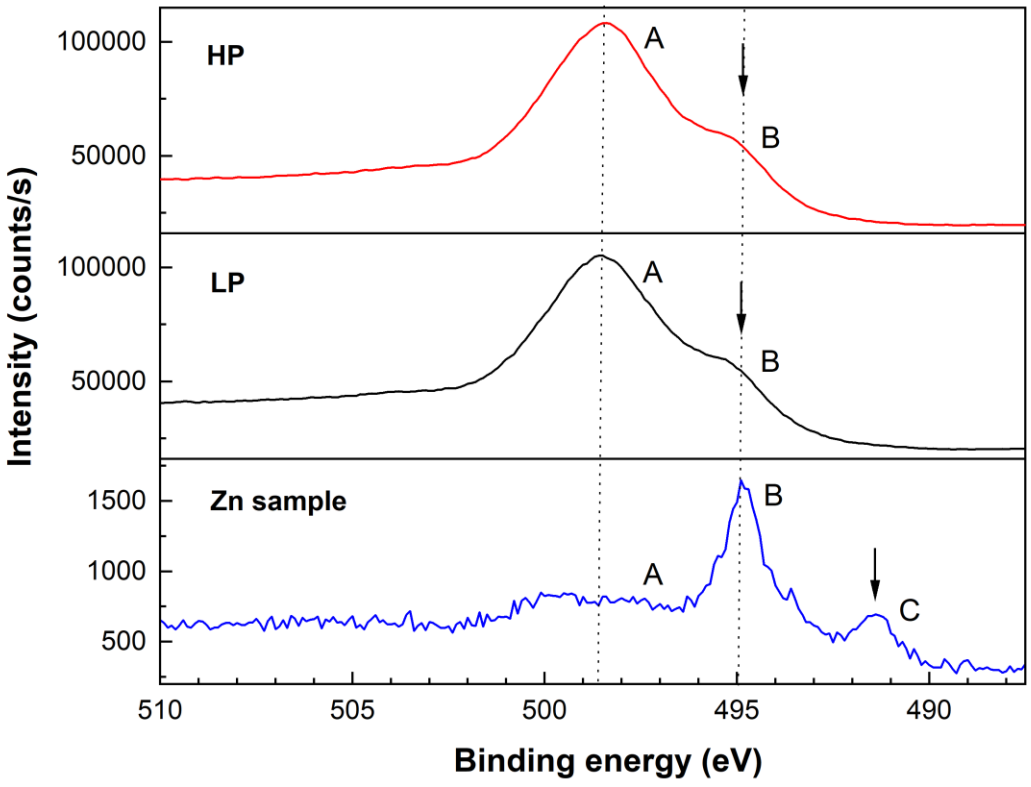
HP
LP
Zn sample
A
B
C
Intensity (counts/s)
Binding energy (eV)
100000
50000
1500
1000
500
510
505
500
495
490

b

Fig. 8

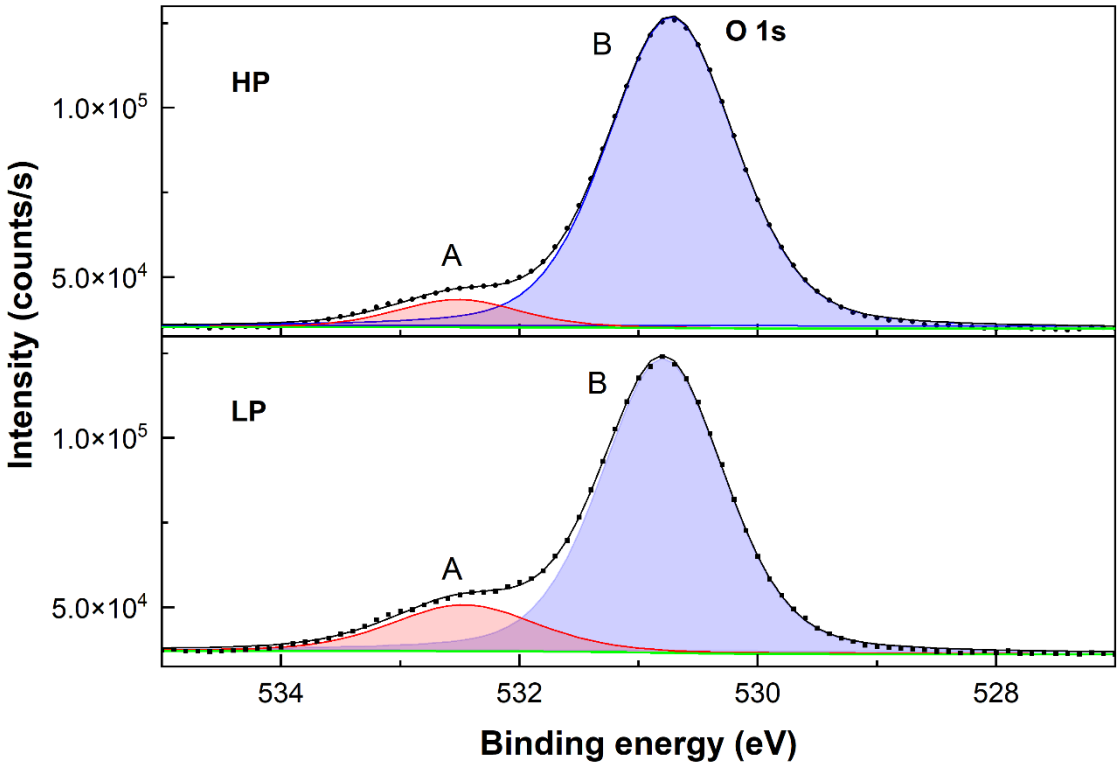
HP
LP
O 1s
A
B
Intensity (counts/s)
1.0×10^5
5.0×10^4
534
532
530
528
Binding energy (eV)

a

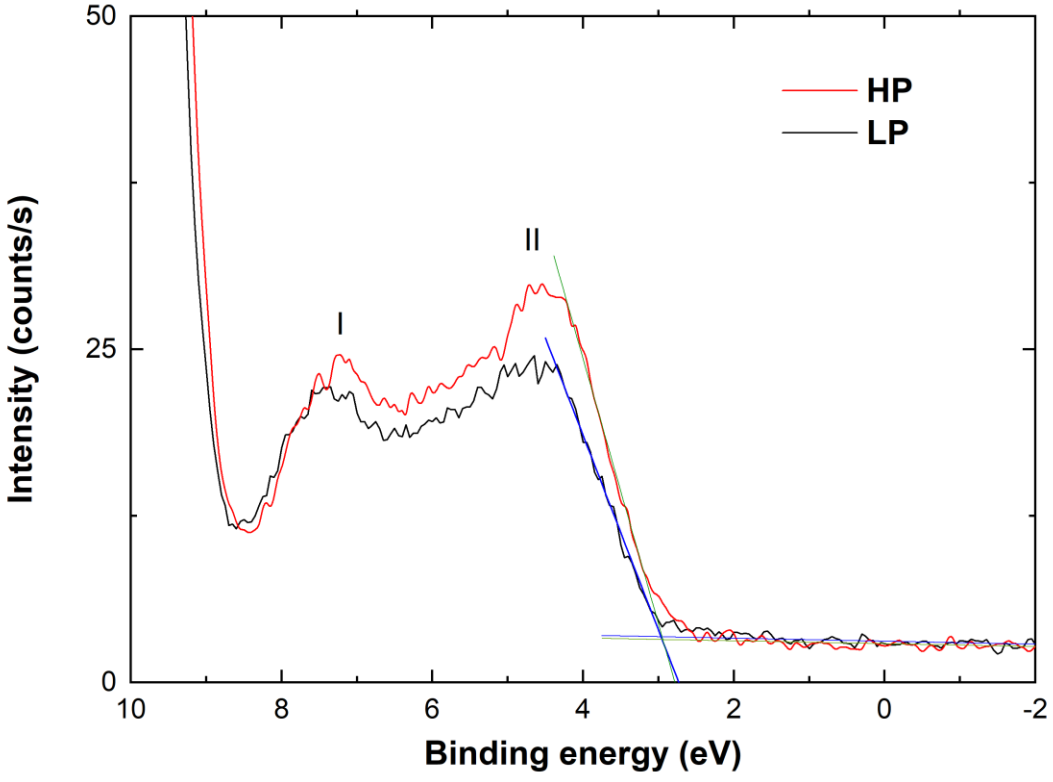
HP
LP
I
II
Intensity (counts/s)
50
25
0
10
8
6
4
2
0
-2
Binding energy (eV)

b

Fig. 9